Stochastic Modeling of Temporal Enhanced Ultrasound: Impact of Temporal Properties on Prostate Cancer Characterization

Layan Nahlawi, *Student Member, IEEE*, Caroline Goncalves, Farhad Imani, Mena Gaed, Jose A. Gomez, Madeleine Moussa, Eli Gibson, Aaron Fenster, *Fellow, IEEE*, Aaron Ward, Purang Abolmaesumi, *Senior Member, IEEE*, Hagit Shatkay*, and Parvin Mousavi*, *Senior Member, IEEE*

***Abstract*—*Objectives*: Temporal Enhanced Ultrasound (TeUS) is a new ultrasound-based imaging technique that provides tissue-specific information. Recent studies have shown the potential of TeUS for improving tissue characterization in prostate cancer diagnosis. We study the temporal properties of TeUS – temporal order and length – and present a new framework to assess their impact on tissue information. *Methods*: We utilize a probabilistic modeling approach using Hidden Markov Models (HMMs) to capture the temporal signatures of malignant and benign tissues from TeUS signals of 9 patients. We model signals of benign and malignant tissues (284 and 286 signals, respectively) in their original temporal order as well as under order permutations. We then compare the resulting models using the Kullback-Liebler divergence and assess their performance differences in characterization. Moreover, we train HMMs using TeUS signals of different durations and compare their model performance when differentiating tissue types. *Results*: Our findings demonstrate that models of order-preserved signals perform statistically significantly better (85% accuracy) in tissue characterization compared to models of order-altered signals (62% accuracy). The performance degrades as more changes in signal-order are introduced. Additionally, models trained on shorter sequences perform as accurately as models of longer sequences. *Conclusion*: The work presented here strongly indicates that temporal order has substantial impact on TeUS performance, thus it plays a significant role in conveying tissue-specific information. Furthermore, shorter TeUS signals can relay sufficient information to accurately distinguish between tissue types. *Significance*: Understanding the impact of TeUS properties facilitates the process of its adopting in diagnostic procedures and provides insights on improving its acquisition.**

***Index Terms*—Hidden Markov Models, Probabilistic modeling, Prostate Cancer, Temporal Enhanced Ultrasound, Temporal Order, Time Domain Signal Analysis.**

I. Introduction

Manuscript received on May 16, 2017; revised on October 6, 2017; accepted on November 17, 2017.

L. Nahlawi is with the School of Computing, Queen's University, Kingston ON, Canada (e-mail: lnahlawi@cs.queensu.ca).

F. Imani and Purang Abolmaesumi are with the Dept. of Electrical and Computer Engineering, University of British Columbia.

M. Gaed, Jose A. Gomez, Madeleine Moussa, Aaron Fenster and Aaron Ward are with the Dept. of Medical Biophysics, Pathology and Robarts Inst., Western University.

E. Gibson is with the Centre for Medical Image Computing, University College London.

H. Shatkay is with the Dept. of Computer and Information Sciences, University of Delaware.

P. Mousavi is with the School of Computing, Queen's University, Kingston ON, Canada.

* H. Shatkay and P. Mousavi have contributed equally to the manuscript.

PROSTATE cancer is the most commonly diagnosed cancer in men, affecting more than 2.9 million people in North America [1], [2]. According to the Canadian Cancer Society, one in eight men is expected to develop prostate cancer in his lifetime [2]. Despite the increased awareness and advances in prostate oncology, the disease remains a prominent health concern for men. The current practice for prostate cancer diagnosis involves measuring the level of Prostate Specific Antigen (PSA) in the blood, along with a Digital Rectal Examination (DRE) to assess the size and stiffness of the prostate gland [3]–[5]. If either test is abnormal, a definitive diagnosis is made using histopathology analysis of core needle biopsy obtained from the prostate under Trans-Rectal Ultra-Sound (TRUS) guidance [6]. Disease prognosis and treatment decisions are based on *grading* – i.e. the assessment of cancer aggressiveness in the biopsy cores [7], [8]. As prostate cancer is heterogeneous, TRUS-guided biopsies result in false negative rate between 30% and 47%, since cancer lesions are often missed, thus repeat biopsies are needed for accurate diagnosis [5], [9], [10]. In addition, cancer grades are underestimated in about 48%, and overestimated in up to 67% of patients [9], [11]. Although prostate cancer screening has led to a 45% decrease in mortality rates, it has also resulted in over-treatment due to the inability of current screening standards to accurately differentiate between indolent and aggressive cancers [12]–[14]. To reduce inaccurate diagnostic rates of TRUS-guided biopsies, a targeted biopsy approach is required, where patient-specific high risk areas of the prostate are sampled. In the past few years, Magnetic Resonance (MR) Imaging [15] and MR-TRUS fusion [16]–[18] have been used for guiding prostate biopsies. However, the ability to obtain accurate diagnosis using ultrasound remains a priority due to the wide availability and relatively low cost of this modality.

Temporal Enhanced Ultrasound (TeUS) has been proposed as a novel ultrasound-based imaging technique for tissue characterization (differentiating between malignant and benign tissues) in prostate cancer [19]–[23]. TeUS has been also used for characterizing *in vitro* animal tissues [19], [24], [25]. Analyzing temporal ultrasound sequences is a promising technique to augment biopsy procedures with tissue-specific information for guiding the needle to areas that are highly likely to be malignant. A TeUS signal is a sequence of ultrasound frames collected during sonication of a stationary tissue over a short period of time - approximately two seconds. These temporal

sequences capture ultrasound echoes from scanned tissue in response to prolonged sonication. During scanning, tissue responses vary from one time point to another, and the typical variation pattern obtained from benign tissue is different from that obtained from malignant one [23]. TeUS has been shown to capture the difference in micro-structure between malignant and benign tissues [26]. Micro-vibration of 1-2 Hz frequency is shown to be the dominant physical phenomenon governing the interaction of TeUS and the scanned tissue. Tissue cellularity is one of the tissue characteristics that affect the echointensity changes conveyed by TeUS. Thus, TeUS provides tissue-specific information that can be used to identify high-risk areas during TRUS-guided biopsies. Cancer likelihood maps can be generated from the analysis of TeUS signals to guide specimen collection, during biopsies, toward focusing on areas more likely to be malignant. Currently, we are working on a GPU implementation of our models to be able to generate and display these maps in real time on ultrasound machines during biopsy procedures.

Most approaches for tissue characterization using TeUS extract features from the signals and use them to build a classification framework. Previously proposed features include the fractal dimension, wavelet coefficients, frequency amplitudes following Discrete Fourier Transform and mean central frequencies, which were used to train support vector machines for tissue characterization in prostate cancer [19]–[21]. More recently, automatic feature extraction using deep-belief networks was proposed for the same purpose [22]. In an earlier retrospective feasibility trial, we introduced a stochastic tissue characterization framework using Hidden Markov Models (HMMs) to explicitly incorporate and model temporal relations that were not taken into account in previous models of TeUS. We demonstrated the feasibility of accurate detection of cancerous ROIs within the biopsy cores [23]. HMMs enable building tissue-specific models that capture the difference between malignant and benign tissue response to prolonged sonication.

Understanding the properties of TeUS is essential for improving data collection and for clinical translation of the technology. Here, we build on our previous work [23], [27] and use HMMs to further examine TeUS signals and assess the impact of their temporal properties, namely order and signal length, on tissue characterization. This work directly investigates the impact of TeUS temporal properties on differentiating tissue types. The temporal order is an important characteristic that demonstrates how tissue-specific information is relayed by TeUS data. Specifically, it is likely to reflect cumulative or repetitive effect (or a combination of both) exerted on the scanned tissue whose response to sonication is recorded. The number of time points in the signal (i.e. the signal length) is another important factor. The impact of change in signal length on TeUS properties can help determine the duration of sonication needed to collect a TeUS signal that carries sufficient information for tissue characterization. The shorter the scanning time, the easier it is to incorporate TeUS-data collection into diagnostic procedures.

HMMs are probabilistic models typically used to detect motifs and patterns in noisy time series [28]. They are widely utilized in machine learning and applied in several domains including speech recognition and synthesis [29], [30]. HMMs have also been used to model biological data such as proteins and DNA sequences [31].

To examine the significance of temporal order, we build HMMs of TeUS signals while conserving their original order as well as under various permutations to their order in time. We use the Kullback-Leiber (KL) divergence [32] to measure the difference between models trained on ordered signals and models trained on signals whose order has been altered. We then compare the performance achieved by the respective models on the target task of tissue-characterization. To assess the impact of signal length, we train HMMs using signal prefixes, where we vary the number of time points included within each prefix (hereinafter referred to as *cropped* signals), and compare the resulting models performance when distinguishing between malignant and benign tissues. We demonstrate that the information carried by the temporal order of TeUS signals is in fact related to tissue malignancy. We also show that accurate differentiation between tissue types can be achieved with shorter TeUS signals, that is, shorter scanning-duration.

In the next section, we present the data and pre-processing of TeUS signals. Section III provides a description of our modeling and tissue characterization framework, and demonstrates our approach for comparing various models. Section IV presents results along with a discussion of their implications. Section V concludes the work and outlines future directions.

II. Temporal Enhanced Ultrasound Data

A. The Dataset

TeUS data comprises time series of ultrasound echo-intensities reflected from a scanned tissue over time. The echo-intensities that ultimately form the ultrasound image of the scanned tissue at each time point are referred to as a Radio-Frequency *frame*. Fig. 1 shows a sequence of 128 ultrasound images corresponding to RF frames obtained during prostate sonography, along with the time-series representation of a typical TeUS signal. In our dataset, each RF frame consists of 1276×64 intensity values (referred to as *RF values*), which amounts to 1276 samples in the axial direction and 64 in the lateral direction as shown in Fig. 2, while the corresponding TeUS time series is 128 frames long. Segmenting the ultrasound images, the boundaries of the prostate are delineated and the echo-intensities corresponding to the organ are located. Fig. 2 shows the prostate boundaries encircled in white. Pre-operatively, *in vivo* ultrasound images were acquired from the prostates of 9 patients who subsequently underwent radical prostatectomy as part of their cancer treatment. A SonixTouch ultrasound machine (Analogic Ultrasound, Massachusetts, USA) was employed to scan the patients using the side-firing transducer of BPL9-5/55 transrectal probe at a frequency of 6.67 MHz. A clinician was holding a motorized cradle, where the probe was mounted. For each patient, the clinician collected a fan of parasagittal B-mode images at intervals of 0.5°, where the size of each pixel was 0.12×0.12 mm. The collected ultrasound images were

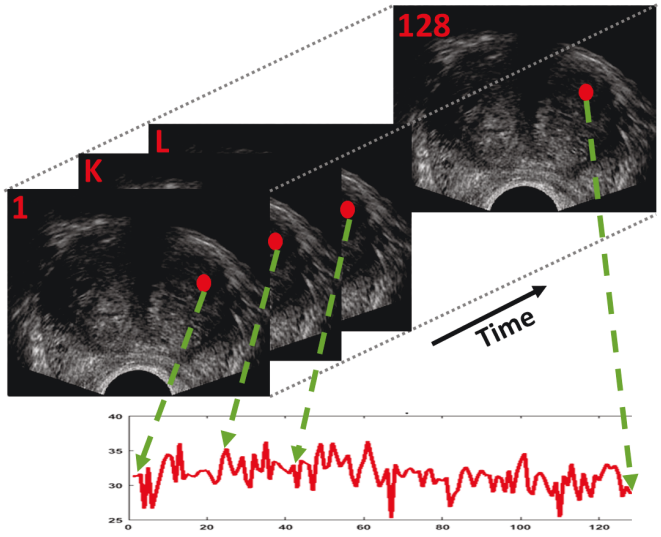

Fig. 1. A Sequence of ultrasound images corresponding to 128 RF frames of a patient's prostate, along with a sample TeUS time series of a given data point in the prostate.

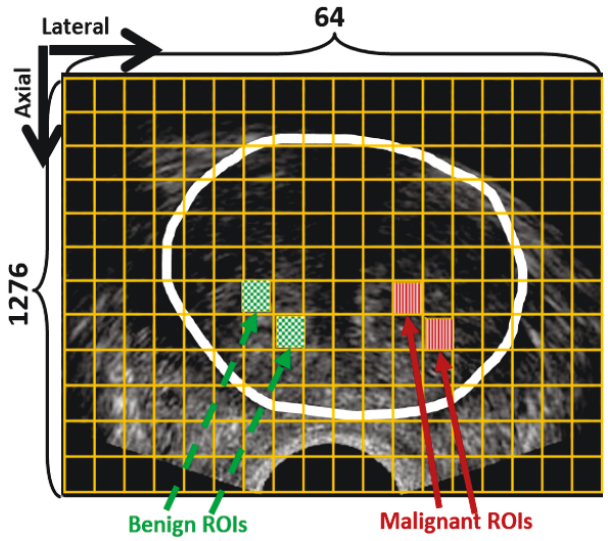

Fig. 2. An example of an RF frame, consisting of 1276 samples in the axial direction and 64 in the lateral direction. The grid divides each RF frame into ROIs. The white circle shows the boundaries of the prostate. The solid red arrows point to ROIs labeled as malignant, while the dashed green arrows point to ROIs labeled as Benign.

then reconstructed into a 3D image with 0.12 mm *isotropic* voxels to be later used during the multi-step registration process performed to establish the ground truth. Afterwards, a fan of 2-dimensional RF frame with a rotational interval of 2° at a resolution of 0.85 mm lateral by 0.04 mm axial directions at a rate of 77 frames/sec [21].

To obtain the ground truth for tissue-characterization, the echo-intensities corresponding to malignant and to benign regions in the prostate were identified using demarcation from postoperative-histopathology analysis of the tissues [33]. The registration of ultrasound images and high-resolution histopathology images is a nontrivial procedure. Thus, MR was used as an intermediary imaging modality. After resection, special fiducials visible in histopathology imaging were implanted in and around the specimens to be used as points of reference later during registration [34]. *Ex vivo* MR images of the organs with fiducials were obtained and the prostates were then sliced into 4.4 mm-thick sections. High-resolution imaging and annotation of the malignant areas was performed by a physician and confirmed by a genitourinary pathologist. Afterwards, 3D reconstruction of the tissue sections was performed [35]. The histopathology information was then overlaid on the *ex vivo* MR images and subsequently registered to the *in vivo* ultrasound images. The registration process performed on this data was previously published by Imani *et al.* [21].

B. Time-domain Representation of TeUS Data

Ultrasound imaging techniques do not provide accurate information about the location of very small objects due to the scattering phenomenon. That is, echo deflected from such small objects in soft tissue is scattered in all directions rather than reflected solely back to the transducer [36]. Thus, the annotation of ultrasound images is based on groups of RF values, (as opposed to single values), corresponding to areas known as *Regions Of Interest* (ROIs), which can be easily visualized by clinicians. Imani *et al.* proposed the use of an ROI size of 1.7×1.7 mm [21], which we also use in this paper. A grid of 1.7×1.7 mm squares is overlaid on each RF frame. The grid divides each frame into ROIs of 44 values in the axial direction and 2 values in the lateral direction. On the ultrasound RF frames, the annotations appear along the line of intersection between the imaging plane and the histopathology cross-section. The ROIs that overlap with the cancerous markings are selected as malignant ROIs and modeled in this study. According to the Epstein criteria, a minimum lesion size of 0.20.5 cc is clinically important [37]. In our dataset, the average size of dominant lesions is 19 mm, with a lower bound of 4 mm. The Gleason Scores (GSs) for the 9 patients vary between 6 and 8. Malignant ROIs were only selected where cancer appears in consecutive histology slices and where the lesion size is > 7 mm. As for benign ROIs, they were selected with a safe margin of ≥ 5 mm away from malignancy, prostatic intraepithelial neoplasia, benign prostatic hyperplasia or atrophy. An example of an ROI grid is depicted in Fig. 2. The ROIs are labeled according to the histopathology annotations registered to the ultrasound. The solid red arrows point to ROIs labeled as malignant, while the dashed green arrows point to ROIs labeled as benign. Each patient data consists of a set of annotated ROIs, in which each ROI is a 128-long series, defined as:

$$ROI_x = \langle ROI_{x_1}, \ldots, ROI_{x_{128}} \rangle, \quad (1)$$

where x enumerates the ROIs, ranging from 1 to 286 for malignant ROIs, and 1-284 for benign ROIs. The total data used here thus consists of 570 ROIs. Within each ROI sequence, the i^{th} value, denoted ROI_{x_i}, is the mean intensity of all 44×2 RF values at the i^{th} time point. As mentioned earlier, due to the scattering phenomenon, single RF values do not accurately represent the image contents, since a single value can be attributed to noise or generated by multiple scatterers.

TABLE I
THE DISTRIBUTION OF MALIGNANT AND BENIGN ROIS OVER PATIENTS, ALONG WITH GSS FOR PRIMARY AND SECONDARY LESIONS PER HISTOPATHOLOGY SLICES.

Patient Number	Number of ROIs		Gleason Scores
	Malignant	Benign	
1	42	42	3+3, 3+4, 4+4
2	17	17	3+3, 3+4, 4+3, 4+4
3	64	61	3+3, 3+4, 4+3, 4+4
4	29	29	3+3, 3+4, 4+4
5	35	35	3+3, 3+4, 4+3, 4+4
6	18	18	3+3, 3+4, 4+4
7	28	29	3+3, 3+4, 4+4
8	30	30	3+3, 3+4, 4+3, 4+4
9	23	23	3+3, 3+4, 4+3, 4+4
Total	286	284	—

As such, averaging the 88 (44×2) RF values into a single mean as we do here, reduces the impact of noise in the TeUS time series without incurring a significant information loss, while also reducing data dimensionality. TeUS Data from the 9 subjects, whose benign and malignant ROIs are clearly labeled, is used in the analysis described here. The ROIs were selected in a way that maximizes the distance between benign and malignant ROIs to avoid mislabeling (see [21] for details regarding the ROI selection process). The number of ROIs per patient, along with GSs of primary and secondary lesions per slice are shown in Table I.

the data is pre-processed to detect any gross-motion using a windowing technique where TeUS signals showing sudden changes in the echointensities are excluded from further analysis. As noted in the introduction, malignant and benign tissues demonstrate different patterns of echointensity variation during the sonication period [19]. As such, patterns of echointensity variations can serve as a source of tissue-specific information carried by TeUS data. To focus the analysis on the variation in values, we calculate the first-order difference series of each ROI_x, transforming the 128-long time series into a 127-long series of differences ROI'_x, where:

$$ROI'_{x_i} = ROI_{x_{i+1}} - ROI_{x_i} \ , \tag{2}$$

and $1 \leq i \leq 127$. Since the first-order difference values ROI'_{x_i} are real numbers while we use discrete observations in our HMMs representation, (see Sec. III-A for details), we discretize these values into 10 equally spaced bins of difference subranges. The ordinal number, O, of each bin is used to represent the values falling in its respective sub-range. As such, the discretized signal is $ROI^d_x = \langle O^k_1, \ldots, O^k_{127} \rangle$, where O^k_1 is the k$^{\text{th}}$ bin number, which is used to represent the value of the first time-point in the difference signal ROI'_x, and $1 \leq k \leq 10$. We experimented with different numbers of bins $(10, 20, \ldots, 50)$, and our experiments suggest that 10 bins are sufficient for effective tissue characterization (see Sec. III-C for further details). The discretized-representations of ROIs, from all patients, are partitioned into two groups: *malignant ROIs* – represented as a (286×127) matrix, $G_{\mathfrak{M}}$, and *benign ROIs* – represented as a (284×127) matrix, $G_{\mathfrak{B}}$. These representations are used to train the HMM models, as discussed in Sec. III.

Order Rearrangement: To assess the significance of order in TeUS signals, we generate collections of order-altered (*rearranged*) ROIs, where we select a block within the sequence (block length ranges between 32 and 128 – the latter being the entire sequence), and permute at random the order of all values within the block. The permutations are performed on the *original signals* before calculating and discretizing the first-order difference. We experimented with blocks of different lengths (32, 64, 96, and 128), and with different starting positions for the block along the sequence (1, 33, 65, or 97). We denote the starting point by f, and the block length by L.

For each of the 10 viable combinations of f and L (that is, the combinations in which $f+L \leq 128$) we generate two rearranged groups of signals: one for malignant ROIs $G^{(f,L)}_{\mathfrak{M}}$ and the other for benign ROIs $G^{(f,L)}_{\mathfrak{B}}$. Fig. 3.A illustrates a simple case where the block-length is 3, the block starting point is I and the end point is K. The values within the rearranged block are permuted at random. Fig. 3.B, 3.C and 3.D show example ROIs in their original order along with a rearranged block of different lengths (L) as well as different first time points (f). For each rearranged group of ROIs $G^{(f,L)}_{\mathfrak{M}}$ and $G^{(f,L)}_{\mathfrak{B}}$, we generate 100 versions, each has a different random permutation of the time points in the rearranged block. We then calculate their first-order difference series and discretize them to be used in training and testing the models of rearranged signals (denoted HMM$^{\text{Re}}$). In total, we generated 2000 ROI groups: 1000 for the malignant ROI groups, $G^{(f,L)}_{\mathfrak{M}}$, and 1000 for the benign ROI groups, $G^{(f,L)}_{\mathfrak{B}}$.

Signal-length Cropping: To determine the effect of the temporal-duration of TeUS signals on tissue characterization, we generated data for collections of *cropped* ROIs while varying signal length. For each signal length, we employed a sliding window of length, z, and a starting-point index, i. The sliding window determines the time points from the original signal to be included in the cropped version of the signal. We experimented with 9 values for the length z, $z \in \{20, 30, \ldots, 100\}$, and 10 values for the starting-point index i, $i \in \{10, 20, \ldots, 100\}$. Combinations of z and i were restricted to those resulting in a window that is fully contained in the original signal. We generated a total of 63 collections of cropped signals. In each collection, the group of malignant ROIs, $G^{(z,i)}_{\mathfrak{M}}$, and the group of benign ROIs, $G^{(z,i)}_{\mathfrak{B}}$, are used to train and test the respective malignant-characteristic and benign-characteristic HMM.

III. METHODS

A. Hidden Markov Models of TeUS Data

An HMM represents a pair of two stochastic processes, where the first process consists of transitions among states that are not directly observable; the states can only be estimated through a second process that generates a sequence of observed symbols [29]. The underlying Markov property assumption implies that the state at time t depends only on the state directly preceding it, that is, the state at time $t-1$, conditionally independent of earlier states. In the work presented here, we use HMMs to model discretized TeUS time series. A hidden Markov model, λ, is formally defined

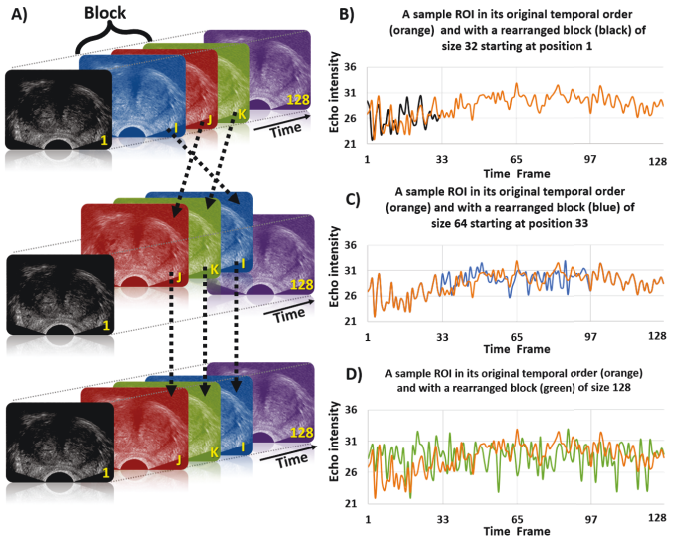

Fig. 3. A) A sequence of ultrasound images corresponding to TeUS data illustrating order rearrangement in a block of length 3 (top). The order of the three frames – I, J and K – is permuted at random (middle), while the whole permuted block is placed at its original position in the sequence (bottom). B-D) A TeUS signal from a sample ROI, shown along with a rearranged block of varying lengths (L) and starting positions (f), where L = 32, 64 and 128 (B, C, D respectively) and f = 33 in C, and 1 in B and D.

using five elements: A set of N states $\{s_1, \ldots, s_N\}$; a set of M observations $\{v_1, \ldots, v_M\}$; a probability distribution governing state-transition denoted by an $N \times N$ matrix A whose elements A_{ij} are defined as:

$$A_{ij} = Pr(s(t+1) = s_j | s(t) = s_i), \tag{3}$$

where $s(t)$ is the state at time point t, $1 \leq i, j \leq N$, $1 \leq t \leq T-1$ and T is the length of the modeled time series; a state-emission probability distribution, denoted by an $N \times M$ matrix B where the elements of B are defined as:

$$B_{ik} = Pr(v = v_K | s = s_i), \tag{4}$$

where v_k is the k^{th} observation symbol, $1 \leq k \leq M$ and $1 \leq i \leq N$ [29]. Typically, the model includes an initial-state distribution, denoted by a $1 \times N$ vector Π, whose elements π_i are defined as: $\pi_i = Pr(s = s_i | t = 1)$, where $1 \leq i \leq N$. However, in our model we assume that s_1 is always the initial state, and as such do not explicitly include the initial vector parameters.

The proposed HMM is ergodic, where transitions between states are expected to capture the pattern of tissue response to prolonged sonication. Based on our experiments, five states (N=5) and ten observations (M=10) have shown to be sufficient for the tissue characterization problem at hand. Hence, the HMM model λ consists of 5 states and 10 observation symbols (see Sec. II-B for details on discretization). The length of the observation sequence is T=127. To train (learn) the model λ using observation sequences $O = \langle o_1, \ldots, o_{127} \rangle$, we estimate the model parameters (namely A & B) to maximize the $log(Pr(O|\lambda))$, which is the log probability of observing sequence O given model λ. Learning the model is an optimization task performed using the Baum-Welch algorithm, an Expectation-Maximization (EM) method. In this method, an initial model is estimated followed by iterative updates of its parameters until convergence is reached to a locally-optimal model.

Model Initialization via Clustering: To initialize the parameters of the HMMs, we use estimates based on clustering the values of the first-order difference signals of ROIs (namely, ROI'_{x_i} as defined in equation 2) into five clusters $\langle C_1, \ldots, C_5 \rangle$, which are centered around randomly initialized centroids c_j, where $1 \leq j \leq 5$*. Each point-value within the ROIs is assigned to one of the clusters according to the squared difference between the ROI'_{x_i} value (see equation 2) and each cluster centroid c_j. The outcome of clustering the values in the malignant ROI matrix $G_{\mathfrak{M}}$ is a 286×127 matrix, $C^{\mathfrak{M}}$, where $C^{\mathfrak{M}}_{ij}$ holds the cluster number (between 1-5) to which the j^{th} value of the i^{th} ROI sequence was assigned. Similarly, clustering the values of the benign ROI matrix $G_{\mathfrak{B}}$ results in a 284×127 matrix, $C^{\mathfrak{B}}$, where each entry in the matrix holds the cluster-number of the cluster into which the respective ROI sequence value was assigned. The parameters of the initial model are estimated based on the values within these matrices. The initial values of the transition matrix A (see Equation 3) and of the observation matrix B (see Equation 4) are thus estimated as:

$$A_{ij} = \frac{\#\text{ of times } C_j \text{ at } (t+1) \text{ \& } C_i \text{ at } t \text{ occurs}}{\#\text{ of times } C_j \text{ occurs}},$$

$$B_{ik} = \frac{\#\text{ of times } v_k \text{ \& } C_i \text{ occurs}}{\#\text{ of times } C_i \text{ occurs}},$$

where C_i and C_j are the i^{th} and j^{th} clusters respectively, $1 \leq i, j \leq 5$, t is the time point, $1 \leq t \leq (T-1)$, v_k is the k^{th} observation symbol in the disretized ROI signal ROI^d_x, and $1 \leq k \leq 10$. Recall that we fix the initial vector Π such that state s_1 is always the initial state in the model, thus π_1=1 and π_i=0 for all $i \neq 1$.

We use the group of malignant ROIs $G_{\mathfrak{M}}$ to learn an HMM $\lambda_{\mathfrak{M}}$ aiming to capture the temporal pattern of signals stemming from malignant tissues, while the group of benign ROIs $G_{\mathfrak{B}}$ is used to learn the HMM $\lambda_{\mathfrak{B}}$ capturing the pattern of signals stemming from benign signals, (we refer to the models as *malignant HMM* and *benign HMM* respectively). The trained models represent the patterns of echointensity variation of tissues as a response to prolonged sonication. To assess the impact of order in the TeUS data, we also train HMMs based on each of the rearranged groups of ROIs, $G^{(f,L)}_{\mathfrak{M}}$ and $G^{(f,L)}_{\mathfrak{B}}$ (see Sec. II-B). Moreover, to assess the effect of signal duration on tissue characterization, we train HMMs using the sets of cropped-ROIs we have generated, both malignant and benign, $G^{(z,i)}_{\mathfrak{M}}$ and $G^{(z,i)}_{\mathfrak{B}}$, respectively.

B. Kullback-Leibler Divergence for HMM Comparison

To assess the impact of the order of points within the TeUS data on the resulting models, we compare the transition and emission probability distributions of the corresponding models built in the previous section. We expect that if the temporal order within the TeUS data carries no information, HMMs learned from ROI sequences in their original order and

*We use the MATLAB implementation of the K-means algorithm.

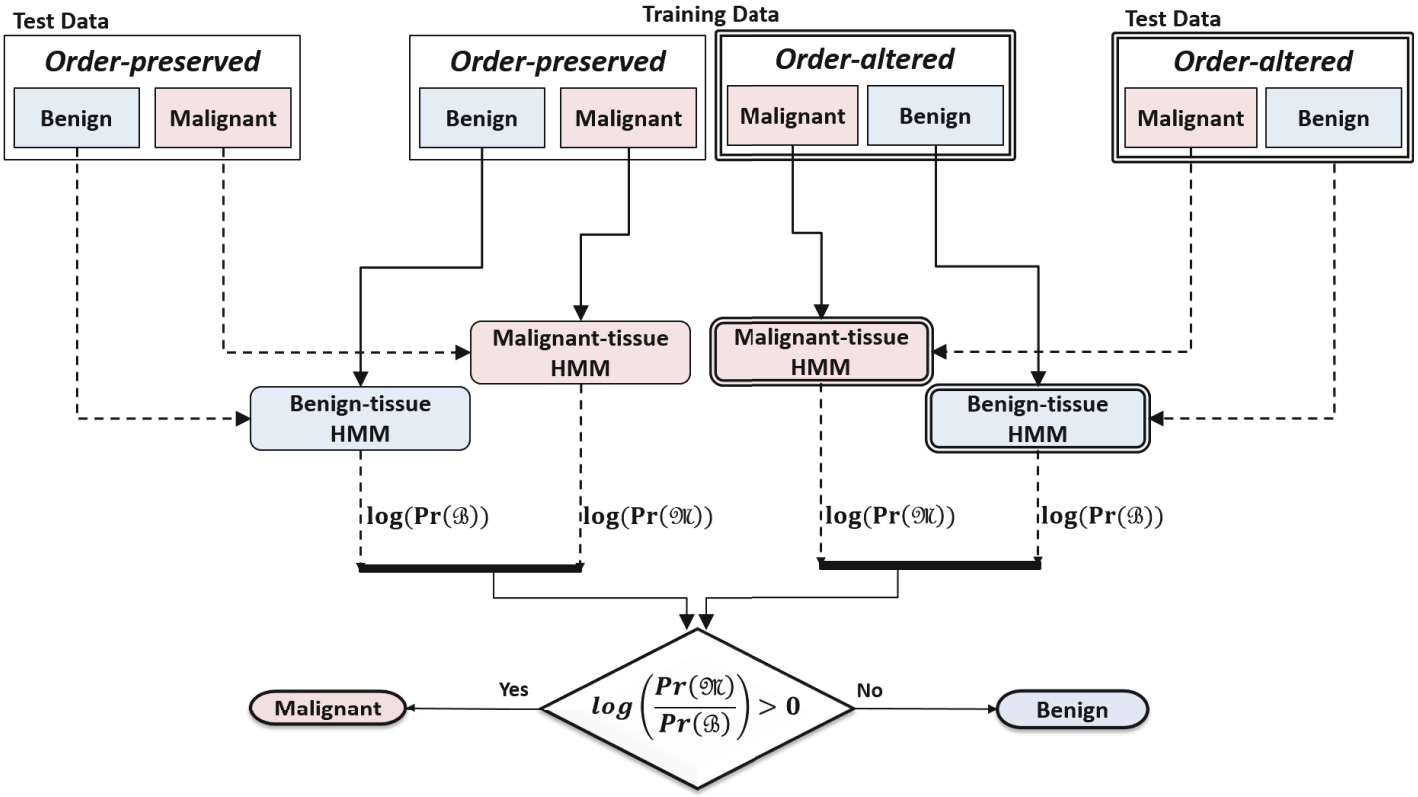

Fig. 4. The tissue characterization framework, which consists of training and testing HMMs based on order-preserving and order-altered signals. The labeling of test-ROI sequences is done according to log of the probability ratio.

models learned from rearranged signals will generate similar sequences with similar governing probability distributions. The similarity in distribution can be measured using the Kullback-Leibler (KL) Divergence [38]. Thus two highly similar models give rise to very small KL-divergence values. Two HMMs are equivalent when the probability assigned by the two models to any observation sequence is the same, and the KL divergence is zero. When two HMMs are not equivalent, the divergence is a positive real number; as the difference between the models increases, the KL-divergence between them increases as well.

To compare two models, λ_i and λ_j, we calculate the symmetric version of the KL-divergence between them [32], [38] utilizing sampled sequences in the calculation. Monte-Carlo sampling is employed to obtain pairs of observation sequences generated from both models. For each pair, a sequence Seq_i is sampled from model λ_i (which was trained on ROIs in their original order), while another sequence of the same length, Seq_j, is sampled from λ_j (the HMM trained on ROIs with permuted order). The symmetric KL-divergence measure, D_s between two models λ_i and λ_j is calculated as:

$$D_s(\lambda_i, \lambda_j) = \frac{D(\lambda_i, \lambda_j) + D(\lambda_j, \lambda_i)}{2},$$

where:

$$D(\lambda_i, \lambda_j) = log(Pr(Seq_i|\lambda_i)) - log(Pr(Seq_i|\lambda_j)),$$

Seq_i is a simulated sequence sampled from model λ_i, and $log(P(Seq_i|\lambda_i))$ and $log(Pr(Seq_i|\lambda_j))$ are the log probabilities of a sequence given the models λ_i and λ_j.

C. Assessing HMM Performance for Tissue Typing

We use a previously proposed tissue characterization framework employing HMMs [23], as depicted in Fig. 4. Supervised learning is utilized to train and test the HMMs, through a leave-one-patient-out cross-validation. In each cross-validation run, the malignant and the benign ROIs of eight out the nine patients serve to train the HMMs and the ROIs of the ninth patient are used for testing. The training and testing are repeated nine times to ensure that the models were tested on the ROIs of all patients. Performance measures are then averaged over the nine cross-validation runs and reported here. For each test-ROI ROI_x^{test}, (where $1 \leq x \leq \#$ of test-ROIs), the *malignant HMM*, $\lambda_{\mathfrak{M}}$, and the *benign HMM*, $\lambda_{\mathfrak{B}}$, generate log likelihood values, $log(Pr(ROI_x^{test}|\lambda_{\mathfrak{M}}))$ and $log(Pr(ROI_x^{test}|\lambda_{\mathfrak{B}}))$, respectively, reflecting how likely each test-ROI is to be generated by each of the HMMs. The ROI test sequence ROI_x^{test} is then assigned the class label Cl_x^{test} based on the log of the probability ratio according to the following:

$$Cl_x^{test} = \begin{cases} \mathfrak{M}, & log\left(\frac{Pr(ROI_x^{test}|\lambda_{\mathfrak{M}})}{Pr(ROI_x^{test}|\lambda_{\mathfrak{B}})}\right) > 0 \\ \mathfrak{B}, & log\left(\frac{Pr(ROI_x^{test}|\lambda_{\mathfrak{M}})}{Pr(ROI_x^{test}|\lambda_{\mathfrak{B}})}\right) \leq 0 \end{cases} \quad (5)$$

If the log ratio is greater than 0, the ROI is labeled *malignant* ($\mathfrak{M}$), otherwise it is labeled *benign* ($\mathfrak{B}$) (see Fig. 4). The HMMs performance in tissue characterization is evaluated by calculating the *accuracy, sensitivity* and *specificity* in predicting the class label of each tissue-type in the test set, defined as:

accuracy=$\frac{TP+TN}{\text{Total \# of ROIs}}$, sensitivity=$\frac{TP}{TP+FN}$, and specificity=$\frac{TN}{TN+FP}$, where *TP* is the number of true positives (i.e. the number of malignant ROIs that were correctly classified), *TN* is the number of true negatives (i.e. benign ROIs that were correctly classified), *FN* is the number of false negatives, and *FP* is the number of false positives. We report the average performance over all cross-validation iterations.

To assess the impact of order on tissue-specific information, we compare the performance of HMMs trained on ROIs in their original order (HMM^{Or}) to that of HMMs trained on ROIs with rearranged order (HMM^{Re}). A better performance of the model trained on the original signals than that obtained by a model trained on permuted sequences, demonstrates that the temporal order is indeed important for capturing tissue-specific patterns. Similarly, we compare the performance of HMMs trained on cropped ROIs of different durations in order to determine the effect of the signal duration (series length) on the ability to distinguish between malignant and benign ROI signals.

D. Experiments

Using ROI sequences in their original temporal order, we have trained two HMMs, one over the sequences originating from malignant tissue (referred to as a *malignant HMM*) and one over those originating from benign tissue (referred to as a *benign HMM*). We then used the groups of rearranged ROI sequences of each type (malignant or benign, described in Sec. II-B), to train a large set of *malignant* and *benign* HMMs, as described below. For each of the 10 viable pairs of *block-length* L and *block starting-position* f, (see Sec. II-B), we generated 100 different random order-permutations of length L, and applied each of these permutations starting at position f to all the malignant originally-ordered sequences. This gives rise to 100 groups of permuted malignant-ROI sequences. Each of these groups is then used to train a respective *malignant HMM*. Notably, this process is repeated 10 times, once for each combination of block-length and starting-point. Through the same permutation process we similarly train *benign HMM*s, each stemming from a set of rearranged benign ROI sequences, under varying permutation block-length and starting point.

We have also generated groups of malignant and benign cropped-ROIs, $G_{\mathfrak{M}}^{(z,i)}$ and $G_{\mathfrak{B}}^{(z,i)}$, where z is the length (duration) of the cropped ROI sequence starting at position i (see Sec. II-B). For each of the 63 viable pairs of duration and starting-position of the sliding window†, The respective group of cropped ROI sequences are used to train 63 *malignant HMM*s and 63 *benign HMM*s.

Using a process of leave-one-patient-out cross validation, we trained *malignant HMM*s and *benign HMM*s over the order-preserved ROI sequences, obtained from malignant and from benign tissue regions, as well as over the order-rearranged ROI sequences and the cropped sequences. For each cross-validation run two HMMs – one for malignant and one for benign – were trained over the respective ROIs obtained from eight of the patients and tested on the ROIs obtained from the ninth patient. Using the trained HMMs, we assigned class labels to ROIs in the corresponding test dataset. We evaluated the performance of each pair of *malignant* and *benign* HMMs by calculating its accuracy, sensitivity and specificity. The performance measures are averaged over the 9 pairs of *malignant* and *benign* HMMs.

†Cropped-ROI length, $z \in \{20, \ldots, 100\}$, and starting position, $i \in \{10, 20, \ldots, 100\}$

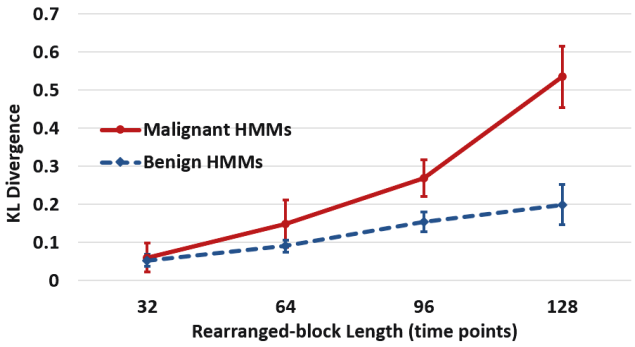

Fig. 5. Average KL-divergence values for divergence calculated between HMMs learned from ordered signals and those trained on rearranged signals. The solid-red line shows the average KL-divergence between models trained on malignant ROI signals, whereas the dashed-blue line shows the KL divergence between models learned from benign ROI sequences.

IV. Results

A. KL-Divergence Results

To compare HMMs trained over the original sequences with those trained over permuted sequences, for each pair $\langle L, f \rangle$ we selected from the respective set of 100 HMMs (be it malignant or benign), the HMM that shows the highest performance in tissue characterization. This selection results in 10 HMMs learned from permuted malignant-ROIs and 10 HMMs learned from benign ones. We calculated the symmetric-sampled KL-divergence $D_s(\lambda_{\mathfrak{m}}, \lambda_{\mathfrak{m}_j})$, between the HMM learned from the malignant ROI sequences in their original order, $\lambda_{\mathfrak{m}}$ and each of the 10 selected models, $\lambda_{\mathfrak{m}_j}$, $(1 \leq j \leq 10)$, learned from rearranged malignant-ROIs. Similarly, we also calculated the KL-divergence $D_s(\lambda_{\mathfrak{b}}, \lambda_{\mathfrak{b}_j})$ between the respective benign models.

For each of the KL-divergence calculations we employed Monte-Carlo sampling to generate sequences, each of length 127, from the respective HMM. KL-divergence values that were obtained from all HMMs learned from permuted ROI sequences sharing the same permutation block-length L (regardless of the block's position f) are averaged. We thus obtain 4 KL-divergence values comparing models of malignant ROIs and 4 values comparing models of benign ROIs. Each KL-divergence value represents the distance between the model trained over ordered ROI sequences and a typical model learned from sequences containing a permuted block of length 32, 64, 96 or 128.

Fig. 5 shows the mean KL-divergence values, as calculated between the models learned from ordered ROIs and each of the models trained on rearranged ROIs, as a function of the rearranged block length L. The red solid-line plots results obtained when the training sequences stem from malignant

regions, while the blue dashed-line corresponds to models trained over sequences stemming from benign tissue. The figure clearly shows that the KL-divergence between models learned from the original sequences and those learned from the permuted ones increases as the number of permutation points increases, indicating that the specific order within the sequences forms an essential component of the signal pattern that is captured by the HMMs.

The increase in KL-divergence is consistent for both models that are trained on malignant ROI sequences and those trained on signals reflected from benign tissue. However, the KL-divergence mean values for malignant models are higher than those obtained from benign models. That is, malignant models appear more sensitive to random rearrangement up to the point where more than 50% of the time points are substituted and none of the original order is retained any more. These results suggest that malignant tissues may be more sensitive to the effect induced by the acoustic waves during sonication, corresponding to a stronger temporal signal in the TeUS sequences. The models compared using KL-divergence are used in our tissue characterization framework. We thus expect that prediction performance of models learned from rearranged sequences stemming from malignant ROIs will be affected more than the performance of models learned from benign ROI sequences, as shown and validated in the next section.

B. Effect of Rearranged-Block Length

During the cross-validation iterations, a total of 18 HMMs were trained (9 models from malignant ROIs and 9 models from benign ROIs) for each of the ordered and permuted ROI groups. We then averaged the performance measures of all HMMs trained on permuted ROIs that share the same rearranged-block length L (regardless of the block's starting position) and used them in assessing the effect of the block length, L, on tissue characterization.

Fig. 6 shows the performance measures of the models trained on order-preserved and order-altered signals as a function of the length of rearranged-blocks. The models of order-preserved signals has zero rearranged frames. The accuracy, sensitivity and specificity decrease as the length of the rearranged-block increases. The accuracy of tissue characterization is 85.01% when using the models trained and tested on ROIs in their original order, whereas it decreases to 62.35% when using the models trained and tested on completely rearranged ROIs ($L=128$ and $f=1$) as shown in Fig. 6.A. This decrease indicates that the temporal order is essential for accurate differentiation between malignant and benign ROIs. The sensitivity decreases from 83.86% for models of ordered signals to 45.12% using models of permuted ROIs (L=128, f=1), whereas the specificity decreases from 86.2% for HMMs of ordered ROIs to 79.6% using the HMMs of the completely rearranged ROIs, as shown in Fig. 6.B and Fig. 6.C respectively.

The results show that order-permutation leads to higher degradation in sensitivity ($\sim$39%) than in specificity ($\sim$7%), which suggests that signal-rearrangement has more impact within the echointensity patterns of malignant ROI sequences than in benign ones. That is, the ordered pattern within the signal is more significant for identifying malignant ROIs than benign ones. These results thus suggest that the mechanism captured by TeUS may be more pronounced in malignant regions than in benign ones.

The specificity levels, which do not fall below 79%, indicate that benign ROIs are correctly identified in the majority of cases even when the signals are completely rearranged. This result indicates that the tissue-specific information characterizing benign regions is not solely reflected by the temporal order of the signal. In contrast, the sensitivity drops to 45% in the rearranged signal, indicating that order is likely to carry tissue-specific information in sequences emanating from malignant regions, which is significant for characterizing the latter.

C. Effect of Rearranged-Block Position

For each of the permuted-ROI groups, both malignant and benign, we also compared the performance among HMMs trained and tested on ROI sequences that have undergone block-permutation for blocks of the same length, L, while varying the block starting position, f, along the ROI sequence. Fig. 7 A-C shows the performance measures obtained from HMMs learned from ROI sequences in which the rearranged block length (L) takes on three different values (32, 64 and 96), while varying the block starting point f along the sequence ($f = 1, 33, 65,$ and 97). The figure demonstrates the impact of the starting position of the rearranged block on performance. Specifically, for all block lengths, both the accuracy and the specificity (A1-C1; A3-C3) are lower when the rearrangement is introduced early in the sequence (e.g. position 1) than when it is introduced toward the end of the sequence (e.g. position 65).

The accuracy and specificity of the model trained on ROIs containing a rearranged block of length 32 at the beginning of the signal is statistically significantly lower than those of models trained on ROI sequences of the same length (L=32) but with different starting points ($f = 33,\ 65$ and 97) (p-value $\ll 10^{-12}$, calculated using a one-tail 2-sample t-test). Moreover, the accuracy and specificity of HMMs learned from ROIs where the rearranged block length was 64 starting at the first point in the signal is statistically-significantly lower than of models learned from ROIs where the permuted block of the same length started at different positions ($f = 33$ and 65) (p-value $\ll 10^{-8}$). The differences in sensitivity across models learned from permuted signals, where the permuted block is of length $L = 32$, or 64, but starts at a different position along the ROI sequence are not statistically significant. As for the models trained on ROIs containing rearranged-blocks of 96 time-points, the accuracy and sensitivity are slightly lower when the starting point of the block f=33, unlike the specificity which is lower when f=1 as shown in Fig. 7.C.

These results implicate that the benign ROIs are more sensitive to rearrangement at the beginning of the signal unlike the malignant ROIs since the decrease in specificity is greater than the decrease in sensitivity when the permuted ROIs have a permuted-block starting at f=1. Hence, the temporal order in the beginning of the signal has more information about the ROIs, in comparison with other parts of the signal.

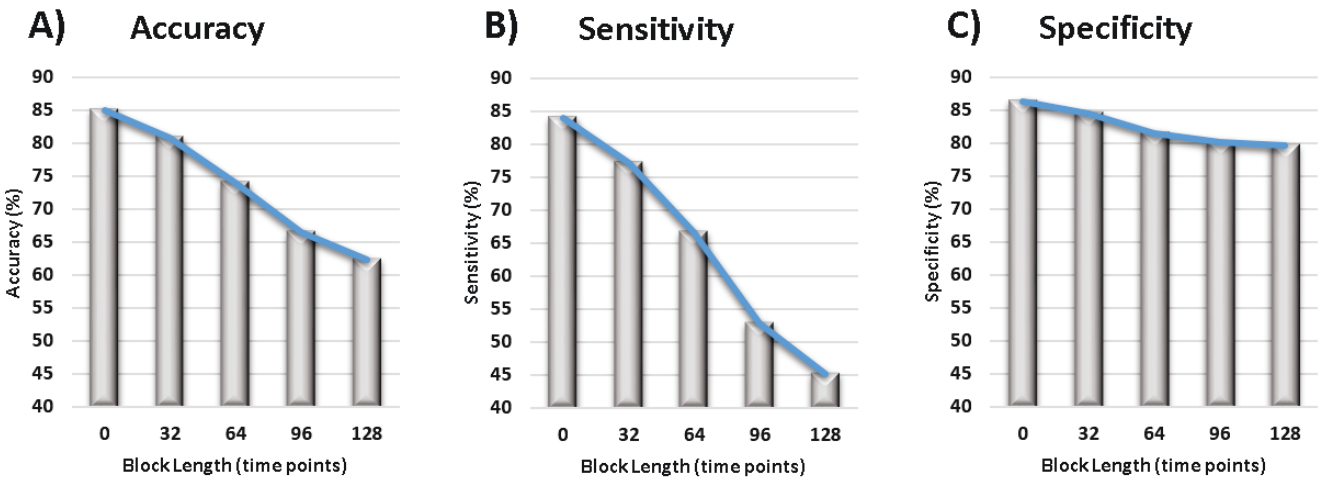

Fig. 6. A comparison between the average performance of HMMs learned from ROIs in their original order (a rearranged-block of length 0) and HMMs trained/tested on ROIs that have a permuted block of length $L \in \{32,64,96,128\}$. Performance is measured in terms of average *accuracy, sensitivity* and *specificity*. Average performance is calculated for all HMMs trained on rearranged sequences sharing the same block-length L regardless of the block starting-position (see Sec. II-B for details).

D. Effect of TeUS Signal Duration

For each of the 63 pairs of malignant and benign models trained on cropped-ROIs, we calculated the average accuracy, sensitivity and specificity, over all HMMs trained on ROIs sequences sharing the same duration, z, regardless of the starting-position, i. Fig. 8 shows the average accuracy, sensitivity and specificity of the resulting HMMs. Standard deviations shown at the top of the bars, indicate variation in performance due to change in the window-starting position i.

As the figure shows, the best performance was attained by HMMs trained on cropped ROIs of length 80, where accuracy was 85.4%. This is almost the same accuracy attained by HMMs trained over the original ordered signals (85.01%, where the signal length is 128). Moreover, the difference in performance between HMMs trained over cropped signals of lengths 80, 90, 100, and 128 are not statistically significant (p-value $\gg 0.05$, using 2-sample t-test). As such, we conclude that HMMs trained over significantly shorter ROI sequences retain the same level of performance as that attained by HMMs trained on the original longer sequences. However, below a certain threshold ($z \leq 70$) performance drops significantly (p-value $<7\times10^{-5}$, according to the one-tailed 2-sample t-test). These results show that shorter ROI signals carry sufficient information about the sequence pattern, to train HMMs that are as effective for tissue characterization as models trained over longer sequences. Thus, the time required for TeUS data collection can be reduced while the resulting sequence can still be used to train effective models for differentiating between malignant and benign signals. The sequences carry tissue specific information captured as repetitive patterns of echointensity changes. These patterns are not captured in signals whose duration fall below a certain threshold, since in the presence of noise, the number of frames in shorter sequences is not sufficient to relay the complete pattern of echointensity changes that is tissue specific.

V. Conclusion

In this paper, we propose a stochastic temporal tissue characterization framework for assessing the influence of temporal-order and signal duration on tissue-specific information relayed by TeUS signals. We utilize HMMs to model TeUS data of malignant and of benign regions obtained from nine prostate cancer patients. Application of HMMs to model the TeUS data (in the time domain), allows us to capture temporal patterns in the signals, and to assess their impact on tissue characterization.

We compare HMMs trained and tested on TeUS data in their original order to those obtained from sequences with permuted order using the symmetric sampled KL-divergence. KL-divergence increases as a function of increased permutation, which indicates that the order of values within the time-domain sequence carries significant information that enables modeling the variability in prostate tissue and the respective variation in tissue response to ultrasound sonication.

To assess the actual impact of TeUS temporal order on tissue characterization in prostate cancer, we compare the performance of HMMs learned from signals in their original temporal order, to that of models learned from order-altered signals. Our results show that the model performance in distinguishing between malignant and benign prostate ROIs decreases as the amount of permutation increases. That is, change in the original order corrupts the tissue-specific pattern of response, reducing the amount of tissue specific information carried by the TeUS signal, and making it harder to distinguish between malignant and benign tissue based on this signal. Moreover, we investigated the effect of the position of permutation along the ROI signals. Our findings demonstrate that HMMs trained on ROIs that undergo permutations at the beginning of their sequences have significantly worse performance than models learned from ROIs containing permuted blocks along other parts of the signals.

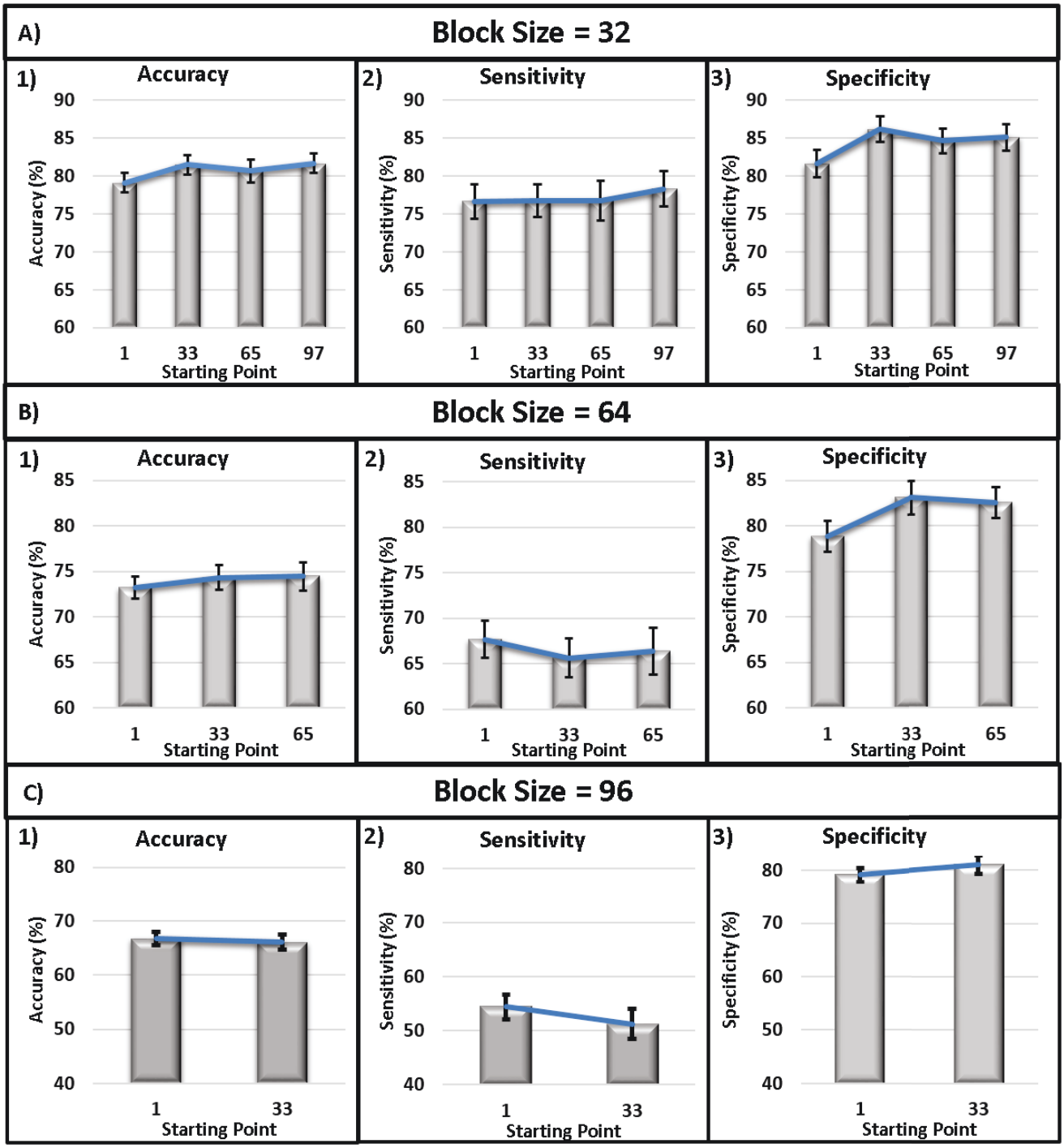

Fig. 7. Average performance resulting from models trained/tested over rearranged ROI sequences that share the same permuted block-length, as a function of the block's starting-point. The standard deviation at the top of the bars shows the variations in the results due to the change in the random permutations used to rearrange the order in the blocks. Parts A-C show the accuracy, sensitivity and specificity for models of ROIs whose rearranged-block length is 32, 64 and 96, respectively.

We also examine the impact of signal duration on tissue-characterization performance, by comparing HMMs trained on cropped TeUS-signals, thus varying signal duration. Our results indicate that even when sequence duration is reduced down to a certain limit (in our dataset, almost 40% reduction in length from 128 to 80), there is sufficient information in the temporal signal to support differentiation between malignant and benign tissue. We note that the experiments, presented here, are designed to show the impact of signal length on the performance of HMMs in tissue typing. For the dataset used in this paper, we demonstrated that 80 frames of data were sufficient to achieve tissue typing with a performance similar

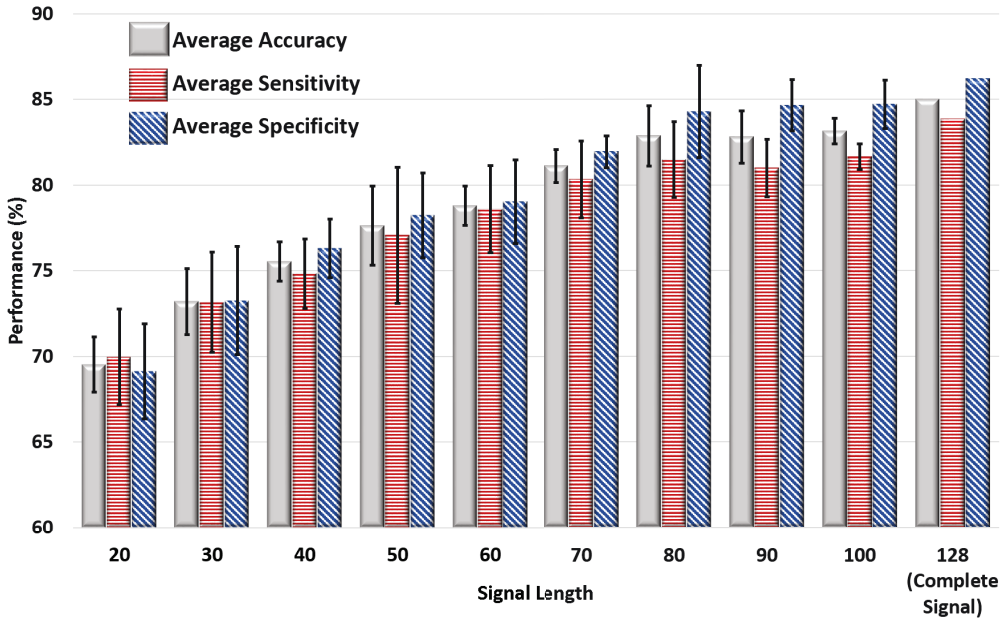

Fig. 8. Average performance (accuracy, sensitivity, and specificity) of HMMs trained on cropped ROI signals, as a function of the signal duration z, along with the results obtained from models trained on the complete signal of length 128. The standard deviation at the top of each of the bars shows the variation in performance due to change in the starting-point index, i, of the sliding window used to generate the cropped signals. The accuracy of the models learned from full-length signals (128) for comparison with performance of HMMs trained on cropped signals. The results of the statistical test show that the accuracy values of the models trained on signals of length 80, or 90, or 100, or 128 are not statistically significantly different from each other.

to that of using the full length of time series. It is important to emphasize that the choice of 80 frames is specific for our data and is likely not a universally optimal signal length. As such, the sonication time needed for gathering sufficient TeUS data can be shortened while retaining the same level of tissue-characterization performance.

These results implicate that the earlier time points in the ROI signals are more informative for tissue characterization, since order-alterations happening later down the signal have a lower impact on the performance than alterations at the beginning and shorter ROI sequences are as effective as longer ones in differentiating between tissue types. To summarize, our findings validate the value of explicitly exploiting temporal order when modelling TeUS signals, and the utility and robustness of such temporal models in distinguishing between malignant and benign tissue. The results of these experiments support further research on tissue characteristics captured by TeUS. The phenomenon governing the interactions between TeUS and the scanned tissues is expected to have a repetitive (periodic) pattern, which is related to changes in the distribution of scatterers within the scanned tissue caused by 1-2 Hz micro-vibrations, as reported by Bayat *et al*. [26]. The time needed to capture the periodic pattern of echointensity changes corresponds to the shortest signal length that is sufficient for tissue typing. It is important to note that showing the feasibility of decreasing the duration of TeUS acquisition enables the clinical translation as it warrants shorter interruption for the current flow of diagnostic procedures.

Acknowledgment

This work was partially supported by grants from NSERC Discovery to Hagit Shatkay and Parvin Mousavi, NSERC and CIHR CHRP to Parvin Mousavi and NIH #R56 lm011354a and NSF IIS EAGER grant #1650851 to Hagit Shatkay.

References

[1] N. Howlader, A. Noone, M. Krapcho, D. Miller, K. Bishop, S. Altekruse, C. Kosary, M. Yu, J. Ruhl, Z. Tatalovich *et al.*, "Seer cancer statistics review, 1975–2013, national cancer institute," *Bethesda, MD http://seer. cancer. gov/csr/1975_2013/. based on November*, 2015.

[2] Canadian Cancer Society and National Cancer Institute of Canada. Advisory Committee on Records and Registries, *Canadian cancer statistics*. Canadian Cancer Society, 2015.

[3] A. Wolf, R. C. Wender, R. B. Etzioni, I. M. Thompson, A. V. D'Amico, R. J. Volk, D. D. Brooks, C. Dash, I. Guessous, K. Andrews *et al.*, "American cancer society guideline for the early detection of prostate cancer: update 2010," *CA: a cancer journal for clinicians*, vol. 60, no. 2, pp. 70–98, 2010.

[4] H. B. Carter, P. C. Albertsen, M. J. Barry, R. Etzioni, S. J. Freedland, K. L. Greene, L. Holmberg, P. Kantoff, B. R. Konety, M. H. Murad *et al.*, "Early detection of prostate cancer: Aua guideline," *The Journal of urology*, vol. 190, no. 2, pp. 419–426, 2013.

[5] H. Huland and M. Graefen, "Changing trends in surgical management of prostate cancer: the end of overtreatment?" *European urology*, vol. 68, no. 2, pp. 175–178, 2015.

[6] N. Mottet, J. Bellmunt, E. Briers, E. U. Association *et al.*, "Guidelines on prostate cancer," *Eur Urol*, vol. 65, no. 1, pp. 124–37, 2014.

[7] J. I. Epstein, L. Egevad, M. B. Amin, B. Delahunt, J. R. Srigley, P. A. Humphrey, G. Committee *et al.*, "The 2014 international society of urological pathology (isup) consensus conference on gleason grading of prostatic carcinoma: definition of grading patterns and proposal for a new grading system," *The American journal of surgical pathology*, vol. 40, no. 2, pp. 244–252, 2016.

[8] J. J. Tosoian, M. Chappidi, Z. Feng, E. B. Humphreys, M. Han, C. P. Pavlovich, J. I. Epstein, A. W. Partin, and B. J. Trock, "Prediction of pathological stage based on clinical stage, serum prostate-specific antigen, and biopsy gleason score: Partin tables in the contemporary era," *BJU international*, 2016.

[9] S. Loeb, M. A. Bjurlin, J. Nicholson, T. L. Tammela, D. F. Penson, H. B. Carter, P. Carroll, and R. Etzioni, "Overdiagnosis and overtreatment of prostate cancer," *European urology*, vol. 65, no. 6, pp. 1046–1055, 2014.

[10] G. A. Sonn, E. Chang, S. Natarajan, D. J. Margolis, M. Macairan, P. Lieu, J. Huang, F. J. Dorey, R. E. Reiter, and L. S. Marks, "Value of targeted prostate biopsy using magnetic resonance–ultrasound fusion in men with prior negative biopsy and elevated prostate-specific antigen," *European urology*, vol. 65, no. 4, pp. 809–815, 2014.

[11] M. C. Cabarrus and A. C. Westphalen, "Multiparametric magnetic resonance imaging of the prostate: a basic tutorial," *Translational Andrology and Urology*, 2017.

[12] J. Herden, D. Schnell, A. Heidenreich, and L. Weissbach, "Mp43-09 "active surveillance" in the everyday care: Results from harow-a prospective, non-interventional study with a mean follow-up of 66.7 months." *The Journal of Urology*, vol. 197, no. 4, p. e557, 2017.

[13] E. A. Singer, A. Kaushal, B. Turkbey, A. Couvillon, P. A. Pinto, and H. L. Parnes, "Active surveillance for prostate cancer: past, present and future," *Current opinion in oncology*, vol. 24, no. 3, pp. 243–250, 2012.

[14] J. S. Jones, *Prostate Cancer Diagnosis: PSA, Biopsy and Beyond*. Springer Science & Business Media, 2012.

[15] C. Tempany, S. Straus, N. Hata, and S. Haker, "Mr-guided prostate interventions," *Journal of Magnetic Resonance Imaging*, vol. 27, no. 2, pp. 356–367, 2008.

[16] D. W. Cool, J. Bax, C. Romagnoli, A. D. Ward, L. Gardi, V. Karnik, J. Izawa, J. Chin, and A. Fenster, "Fusion of mri to 3d trus for mechanically-assisted targeted prostate biopsy: system design and initial clinical experience," in *International Workshop on Prostate Cancer Imaging*. Springer, 2011, pp. 121–133.

[17] P. A. Pinto, P. H. Chung, A. R. Rastinehad, A. A. Baccala, J. Kruecker, C. J. Benjamin, S. Xu, P. Yan, S. Kadoury, C. Chua *et al.*, "Magnetic resonance imaging/ultrasound fusion guided prostate biopsy improves cancer detection following transrectal ultrasound biopsy and correlates with multiparametric magnetic resonance imaging," *The Journal of urology*, vol. 186, no. 4, pp. 1281–1285, 2011.

[18] G. A. Sonn, S. Natarajan, D. J. Margolis, M. MacAiran, P. Lieu, J. Huang, F. J. Dorey, and L. S. Marks, "Targeted biopsy in the detection of prostate cancer using an office based magnetic resonance ultrasound fusion device," *The Journal of urology*, vol. 189, no. 1, pp. 86–92, 2013.

[19] M. Moradi, P. Mousavi, A. H. Boag, E. E. Sauerbrei, D. R. Siemens, and P. Abolmaesumi, "Augmenting detection of prostate cancer in transrectal ultrasound images using SVM and RF time series," *IEEE Transactions on Biomedical Engineering,*, vol. 56, no. 9, pp. 2214–2224, 2009.

[20] M. Aboofazeli, P. Abolmaesumi, G. Fichtinger, and P. Mousavi, "Tissue characterization using multiscale products of wavelet transform of ultrasound radio frequency echoes," in *Engineering in Medicine and Biology Society, 2009. EMBC 2009. Annual International Conference of the IEEE*. IEEE, 2009, pp. 479–482.

[21] F. Imani, P. Abolmaesumi, E. Gibson, A. Khojaste, M. Gaed, M. Moussa, J. A. Gomez, C. Romagnoli, M. Leveridge, S. Chang *et al.*, "Computer-aided prostate cancer detection using ultrasound rf time series: In vivo feasibility study," *Medical Imaging, IEEE Trans on*, vol. 34, no. 11, pp. 2248–2257, 2015.

[22] S. Azizi, F. Imani, S. Ghavidel, A. Tahmasebi, J. T. Kwak, S. Xu, B. Turkbey, P. Choyke, P. Pinto, B. Wood *et al.*, "Detection of prostate cancer using temporal sequences of ultrasound data: a large clinical feasibility study," *International journal of computer assisted radiology and surgery*, vol. 11, no. 6, pp. 947–956, 2016.

[23] L. Nahlawi, F. Imani, M. Gaed *et al.*, "Prostate cancer: Improved tissue characterization by temporal modeling of radio-frequency ultrasound echo data," in *Proceedings of the International Conference on Medical Image Computing and Computer Assisted Intervention.*, 2016.

[24] M. Moradi, P. Mousavi, and P. Abolmaesumi, "Tissue characterization using fractal dimension of high frequency ultrasound rf time series," in *International Conference on Medical Image Computing and Computer-Assisted Intervention*. Springer Berlin Heidelberg, 2007, pp. 900–908.

[25] F. Imani, P. Abolmaesumi, M. Daoud, M. Moradi, and P. Mousavi, "Tissue classification using depth-dependent ultrasound time series analysis: in-vitro animal study." *International Society for Optics and Photonics (SPIE) Publications (Electrical and Computer Engineering)*, 2011.

[26] S. Bayat, F. Imani, C. D. Gerardo, G. Nir, S. Azizi, P. Yan, A. Tahmasebi, S. Wilson, K. A. Iczkowski, M. S. Lucia *et al.*, "Tissue mimicking simulations for temporal enhanced ultrasound-based tissue typing," in *SPIE Medical Imaging*. International Society for Optics and Photonics, 2017, pp. 101 390D–101 390D.

[27] L. Nahlawi, F. Imani, M. Gaed, J. A. Gomez, M. Moussa, E. Gibson, A. Fenster, A. D. Ward, P. Abolmaesumi, P. Mousavi *et al.*, "Using hidden markov models to capture temporal aspects of ultrasound data in prostate cancer," in *BIBM, 2015 IEEE Int. Conf. on*. IEEE, 2015, pp. 446–449.

[28] L. R. Rabiner and B.-H. Juang, "An introduction to hidden markov models," *ASSP Magazine, IEEE*, vol. 3, no. 1, pp. 4–16, 1986.

[29] L. Rabiner, "A tutorial on hidden markov models and selected applications in speech recognition," *Proceedings of the IEEE*, vol. 77, no. 2, pp. 257–286, 1989.

[30] K. Tokuda, Y. Nankaku, T. Toda, H. Zen, J. Yamagishi, and K. Oura, "Speech synthesis based on hidden markov models," *Proceedings of the IEEE*, vol. 101, no. 5, pp. 1234–1252, 2013.

[31] R. Hughey and A. Krogh, "Hidden markov models for sequence analysis: extension and analysis of the basic method," *Computer applications in the biosciences : CABIOS*, vol. 12, no. 2, pp. 95–107, Apr 1996.

[32] B.-H. F. Juang and L. R. Rabiner, "A probabilistic distance measure for hidden markov models," *AT&T technical journal*, vol. 64, no. 2, pp. 391–408, 1985.

[33] F. J. Bianco, P. T. Scardino, and J. A. Eastham, "Radical prostatectomy: long-term cancer control and recovery of sexual and urinary function ("trifecta")," *Urology*, vol. 66, no. 5, pp. 83–94, 2005.

[34] A. D. Ward, C. Crukley, C. A. McKenzie, J. Montreuil, E. Gibson, C. Romagnoli, J. A. Gomez, M. Moussa, J. Chin, G. Bauman *et al.*, "Prostate: registration of digital histopathologic images to in vivo mr images acquired by using endorectal receive coil," *Radiology*, vol. 263, no. 3, pp. 856–864, 2012.

[35] E. Gibson, C. Crukley, M. Gaed, J. A. Gómez, M. Moussa, J. L. Chin, G. S. Bauman, A. Fenster, and A. D. Ward, "Registration of prostate histology images to ex vivo mr images via strand-shaped fiducials," *Journal of Magnetic Resonance Imaging*, vol. 36, no. 6, pp. 1402–1412, 2012.

[36] W. R. Hedrick, D. L. Hykes, and D. E. Starchman, *Ultrasound physics and instrumentation*. Elsevier Mosby, 2005.

[37] S. F. Oon, R. W. Watson, J. J. OLeary, and J. M. Fitzpatrick, "Epstein criteria for insignificant prostate cancer," *BJU international*, vol. 108, no. 4, pp. 518–525, 2011.

[38] S. Kullback and R. A. Leibler, "On information and sufficiency," *The annals of mathematical statistics*, vol. 22, no. 1, pp. 79–86, 1951.